CREATION OF CRACKS OF KNOWN SIZES IN REINFORCED CONCRETE BEAMS AND PERFORMANCE EVALUATION OF SILANE IN CONCRETE BRIDGE DECKS

By

SYED MUHAMMAD AQIB

Bachelor of Science in Civil Engineering

National University of Sciences and Technology

Islamabad, Pakistan

2016

Submitted to the Faculty of the
Graduate College of the
Oklahoma State University
in partial fulfillment of
the requirements for
the Degree of
MASTER OF SCIENCE
May, 2020

CREATION OF CRACKS OF KNOWN SIZES IN REINFORCED CONCRETE BEAMS AND PERFORMANCE EVALUATION OF SILANE IN CONCRETE BRIDGE DECKS

Thesis Approved:

Dr. Norbert J. Delatte

Thesis Adviser

Dr. Julie Ann Hartell

Dr. Deb Mishra

ACKNOWLEDGEMENTS

I am grateful to my beloved parents who nurtured me and continued to support me throughout every step of my life. I am indebted to my wife **Sara Sultan** for her priceless help and tremendous support.

I would like to express special gratitude to my advisors **Professor Dr. Norbert J. Delatte** and **Professor Dr. M. Tyler Ley** for their support and mentorship throughout my master's degree. Their guidance and advice had been instrumental and pivotal and gave me inspiration as I navigated the challenges of my academic career.

I am profusely thankful to **Dr. Julie Ann Hartell** and **Dr. Deb Mishra** for serving as a member on my graduate committee as well as providing me with valuable feedback and helping me improve the quality of my work significantly.

I would especially like to thank **Amir Behravan** for his much valued help during my research and conducting experimental work for the second part of my thesis, and I am thankful to fellow graduate student **Michael Dickey** for his help with the experimental setup for the first part of my thesis at the Bert's Cooper Lab in civil engineering department.

I am grateful to **Oklahoma Department of Transportation** for providing funding for this project.

Finally, I am thankful to all the individuals who have rendered valuable assistance to my study. Many thanks to the friends I have made and time I have spent with during my years at Oklahoma State University.

Name: SYED MUHAMMAD AQIB

Date of Degree: MAY, 2020

Title of Study: CREATION OF CRACKS OF KNOWN SIZES IN REINFORCED CONCRETE BEAMS AND PERFORMANCE EVALUATION OF SILANE IN CONCRETE BRIDGE DECKS

Major Field: CIVIL ENGINEERING

Abstract:
Cracks are a major concern for the durability of concrete as they allow the harmful chemicals from outside to penetrate the concrete surface. Investigating the effect of various crack sizes is vital to further evaluate the surface treatments' performance. In this research, a novel technique is developed to create cracks of known size consistently in reinforced concrete beams using a very simple methodology which applies direct tensile load that cracks the beam. A variety of crack sizes is created ranging from very small (<1/100 inch [*0.25 mm*]) up to ½ inch [*12.7 mm*] and based on the results, a simple process is outlined which can be used to create predetermined crack sizes consistently. Silane is investigated as a surface treatment material, using Transmission X-ray Microscopy (TXM) and Optical Staining Techniques. The TXM results revealed that samples with silane coatings exhibited eight and half times less penetration of outside chemicals as compared to non-silane samples at a depth of 2 mm. In some samples, defects on the surface of the silane coating such as cracks, caused the coating to lose its efficiency. Quantitative measurements made using optical staining techniques show that silane thickness for all the 14 samples was 2.5 mm. This work shows in field applications that silanes are a useful and practical tool to significantly reduce the permeability of concrete.

TABLE OF CONTENTS

Chapter Page

LIST OF TABLES

Table Page

LIST OF FIGURES

Figure Page

CHAPTER I

CREATION OF CRACKS OF KNOWN SIZES IN REINFORCED CONCRETE BEAMS

1.1 Introduction

Cracks in concrete are a major concern for durability problems primarily because they let the harmful chemicals such as chlorides, into the concrete matrix. This can cause concrete deterioration mechanisms such as corrosion of steel reinforcement, freeze-thaw damage, alkali-silica reaction, and salt-scaling, which can render the structures and bridges out of service causing severe monetary and infrastructure losses (PCI 2002; T. M. Ley et al. 2012; Khanzadeh Moradllo et al. 2015; Mehta 1991; Koch et al. 2002; Basham et al. 1995). Therefore, it is necessary to quantitatively study the effect of cracks on the durability and long-term performance of concrete.

There are several tests available that create cracks in concrete to achieve a variety of objectives. Traditional flexural tests such as third-point loading (ASTM C78 2018) and center-point loading (ASTM C293 2016) tests induce flexural cracks in a beam in the bottom fiber to estimate the flexural strength of concrete. Compact tension tests such as disk-shaped compact tension test (ASTM D7313 2013; Amirkhanian et al., n.d.) and modified compact tension test (Fernández-Canteli et al. 2014; Cifuentes et al. 2017), wedge splitting test (Guan et al. 2017; Löfgren et al., n.d.; Brohwiler et al. 1990; Abdalla et al. 2003), and three-point bending test on notched beams (Bordelon 2008; Zhang et al. 2015; Amirkhanian et al., n.d.) are used to estimate the fracture

properties by inducing a notched crack and calculating the crack mouth opening displacement (CMOD).

All the above-mentioned test methods create cracks in concrete in some way, but the size of these cracks is not known beforehand. If a crack size of a known width is needed, these tests cannot be used.

A procedure was designed by Virginia Department of Transportation (VDOT) to induce crack sizes of known width by placing rectangular shims made up of filter papers in the molds of specimens before placing the concrete. After the concrete had been placed and hardened, these shims would either be removed or remain inside and dissolve, and this would create an open space left by the removal of shims which would be utilized as a crack for further testing. Using this procedure, crack sizes in the range of 0 inch to 0.01 inch [*0.25mm*] were created (Torkornoo et al. 2018).

Wiggenhauser et al. designed a procedure based on using expanding mortar in a series of blind holes, to create reproducible and controlled cracks in concrete. To direct the crack development and control the depth, reinforcement alignment was used. The method needs to be more adequate since the cracks produced were very different from the actual cracks in concrete and hence they were not useful enough to investigate further (Wiggenhauser et al. 2018).

Cracks could be instilled in concrete in many ways by applying force, but it needs to be controlled to create stable and consistent cracks (Wiggenhauser et al. 2018). This work establishes a novel technique to create cracks of required size consistently using a very simple and basic methodology in reinforced concrete. This technique can be used to create cracks of a predetermined size which can be used in various testing procedures to see the effect of crack sizes on durability mechanisms.

1.2 Experimental Methods

1.2.1 Sample Preparation

A total of 26 notched beams were prepared with a typical mixture design used in concrete bridge decks (shown in Chapter II: Table II- 1). Fly ash was used at a 20% replacement and the water-to-cementitious ratio was 0.45. The mix design is shown in Table I- 1. Each beam was demolded after two days of mixing and then it was placed in a fog room for moisture-curing for one day. After three days of mixing, the beams were broken as described below.

Table I- 1: Mix design of all samples

Cement	**Fly Ash**	**Coarse Aggregate (#57)**	**Fine Aggregate**	**Water**	**w/cm ratio**
lb/yd^3 *kg/m^3*	lb/yd^3 *kg/m^3*	lb/yd^3 *kg/m^3*	lb/yd^3 *kg/m^3*	lb/yd^3 *kg/m^3*	
488 *290*	122 *73*	1835 *1089*	1195 *709*	275 *163*	0.45

The dimensions of the beams were 6 inches [*152 mm*] in depth and width, and 20 inches [*508 mm*] in length. A #4 deformed steel reinforcement is placed in the middle from the sides and middle of the thickness. A notch is placed in the top and bottom of the beam using steel plates. A schematic diagram is shown in Figure I- 1.

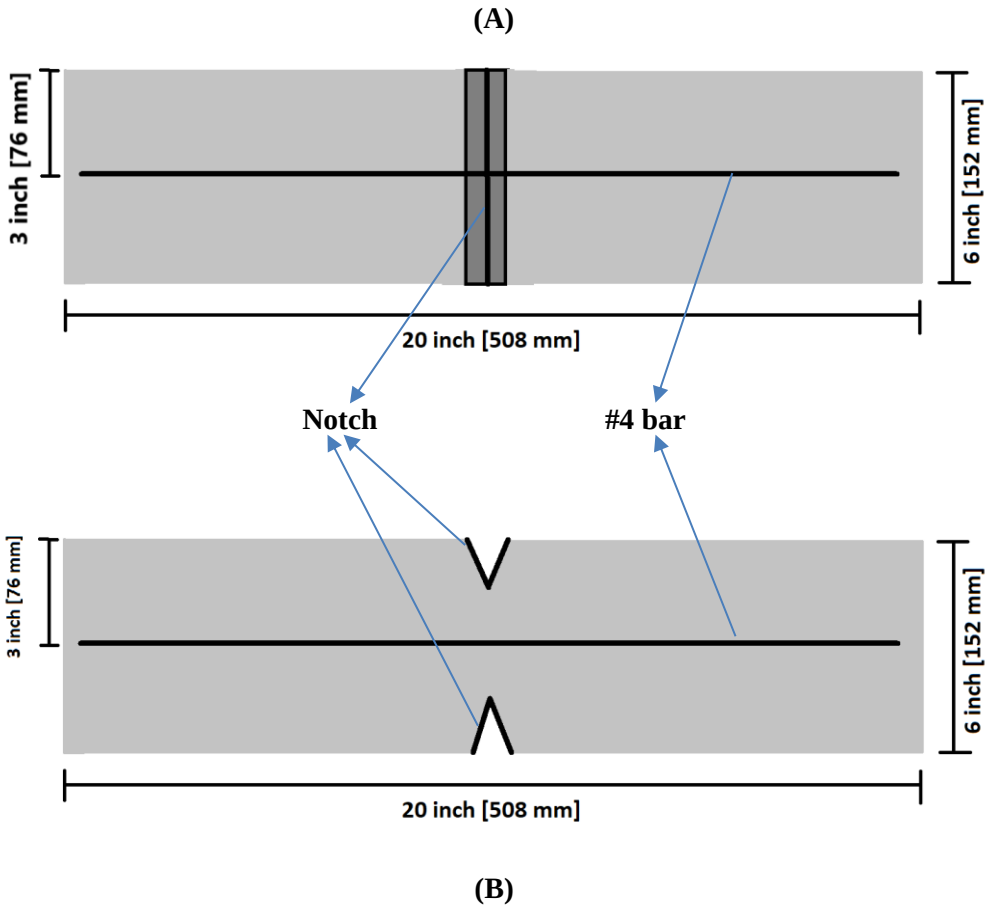

Figure I- 1:Schematic diagram of notched-beam showing dimensions and placement of steel reinforcement (A) Top and bottom view (B) Side view

1.2.2 Testing Methodology

The hydraulic testing frame of a universal testing machine called "Instron 1500HDX" is used to create cracks in the beam. As shown in Figure I- 2, the loading heads are mounted on the Instron, one up and one down, and the beam is placed between them. At this point, the steel notches are still embedded in the beam.

The testing methodology is explained for one beam. During the test, the top loading head does not move, and the bottom loading head moves up which applies a tensile load to the beam and when the tensile stress exceeds the tensile strength of concrete, the beam cracks. The distance that the bottom loading head moves up is called "*cross-head displacement*" but for simplicity, this will be

referred to as “displacement” throughout this chapter. The displacement and the load applied are automatically measured by the Instron’s Data Acquisition System (DAQ) and displayed on the computer screen.

Figure I- 2: Assembly of Instron 1500 HDX with the beam mounted on loading heads

Figure I- 3:Crack propagation in beams

This is a load-controlled test and the load rate is 450 pounds (lbs.) per minute. After every 500 lbs., the Instron is programmed to pause for 30 seconds, hold the current displacement, and do not apply more load. During this pause, the displacement and the load are noted from the computer screen and the size of the crack opening is measured manually using a crack card at three different locations (A, B, C) at the front and three at the back face of the beam as shown in Figure I- 3. This gives a total of six measurements for each beam per every 500 lbs. loading interval.

This scheme of 500 lbs. load followed by 30 seconds pause, another 500 lbs. load followed by another 30 seconds pause is carried on until the ending parameter is reached. The test is stopped at this point and the Instron does not apply more load and maintains the current displacement which means the beam is still under load. The crack size at six locations is measured at this stage and the mean value of these six measurements is called "*initial crack size*".

After that, the beam is unloaded, taken off the loading assembly and then the crack size is measured again at the same six locations on both faces. The mean value of these six measurements is called "*final crack size*". After this, the beam is discarded.

The testing methodology is shown in Figure I- 4.

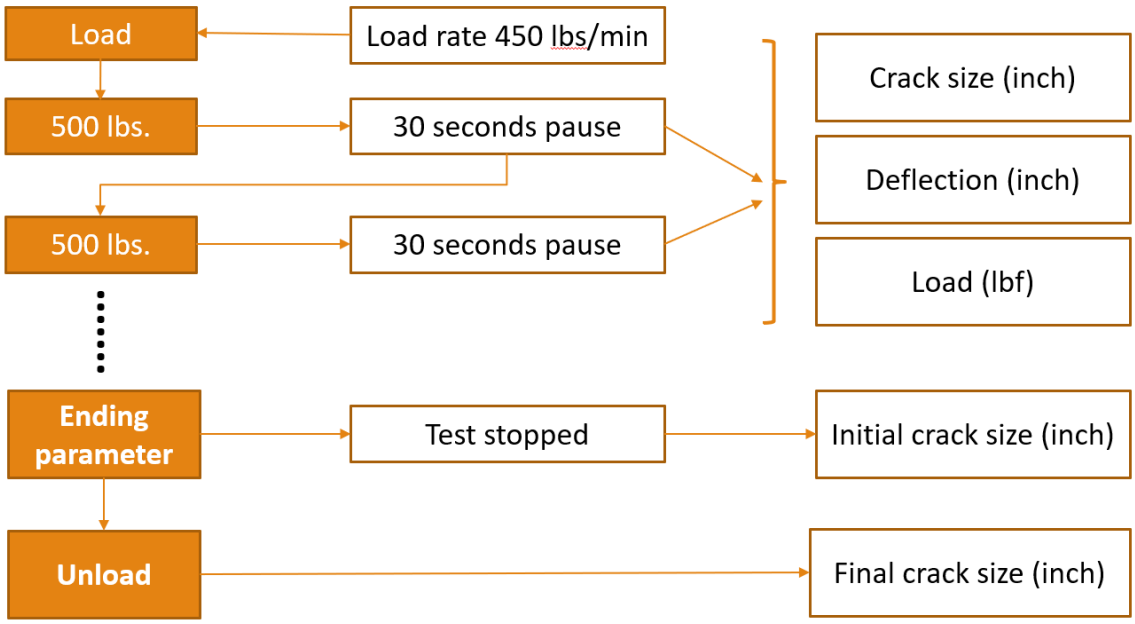

Figure I- 4: Testing methodology schematic

Although this test is load-controlled which means that the Instron tries to maintain the specified load rate, the load (lbf) was somewhat unpredictable. The plots shown in Figure I- 5 are for one beam only but these trends were observed in all the beams. As shown in Figure I- 5 (A), the variation in load as the displacement increases is very unpredictable and therefore, the load was not used as the ending parameter to avoid errors. However, the variation in crack size as displacement increased is a very strong linear trend as shown in Figure I- 5 (B). Hence, the displacement was used as ending parameter to determine when the test should be stopped.

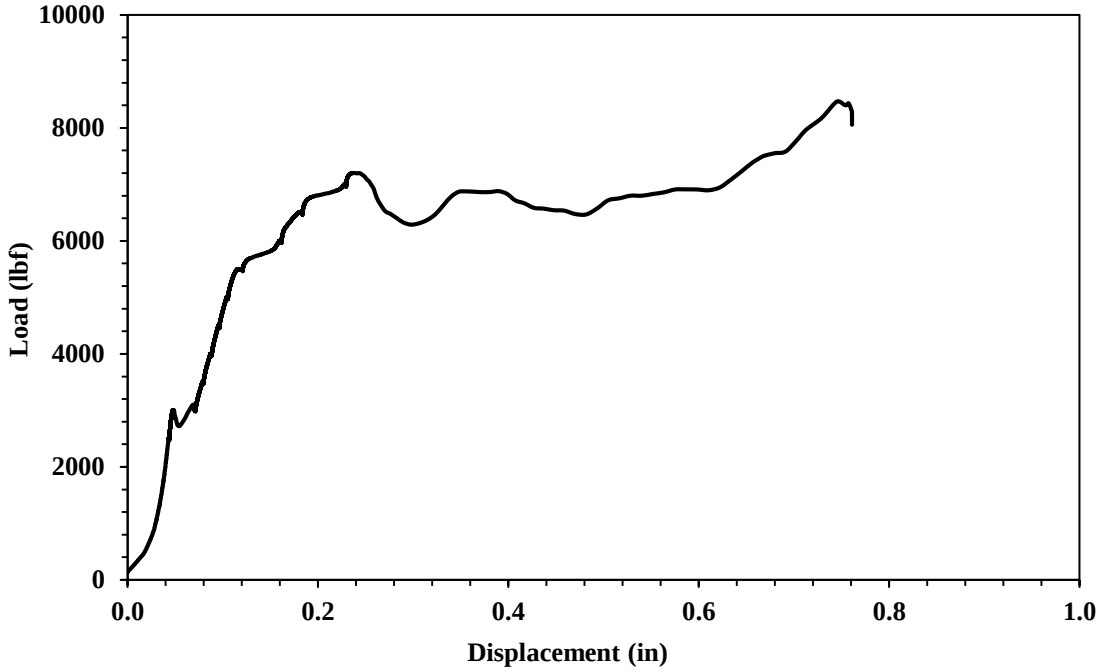

(A)

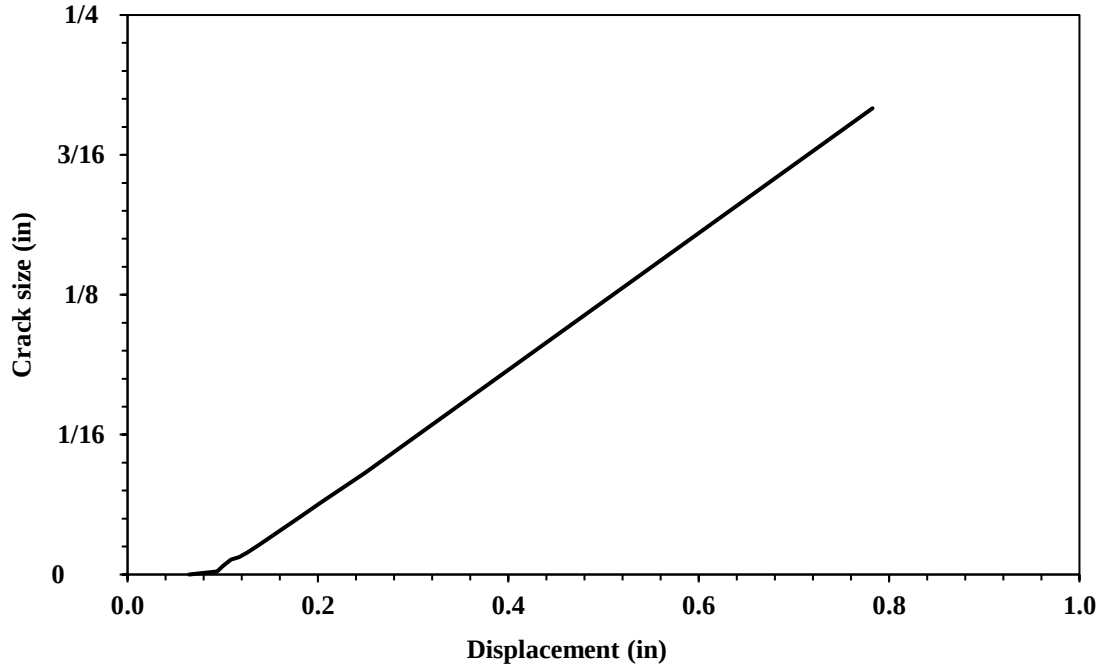

(B)

Figure I- 5: (A) Load vs. displacement (B) Crack size vs. displacement [1 inch = 25.4 mm]

Final cracks up to a width of ½ inch [*12.7 mm*] were created and analyzed in this work. To get a variety of final crack sizes covering a range from very small up to ½ inch [*12.7 mm*], the displacement at which the test was stopped for a particular beam was varied from as small as 0.14 inch [*3.6 mm*] to 2 inch [*50.8 mm*]. Since smaller displacements produce smaller final crack sizes and vice versa, an assortment of final crack sizes was obtained. For 20 beams, the test was stopped when the displacements was less than 1 inch [*25.4 mm*] and for the rest, the displacements was between 1 inch [*25.4 mm*] and 2 inch [*50.8 mm*].

1.2.3 Stress in steel reinforcement and concrete using Mechanics

The stress is calculated in steel reinforcement and concrete using mechanics principles. A free-body diagram of the portion highlighted in red circle in Figure I- 6(A) is shown in Figure I- 6(B) that approximates the actual conditions.

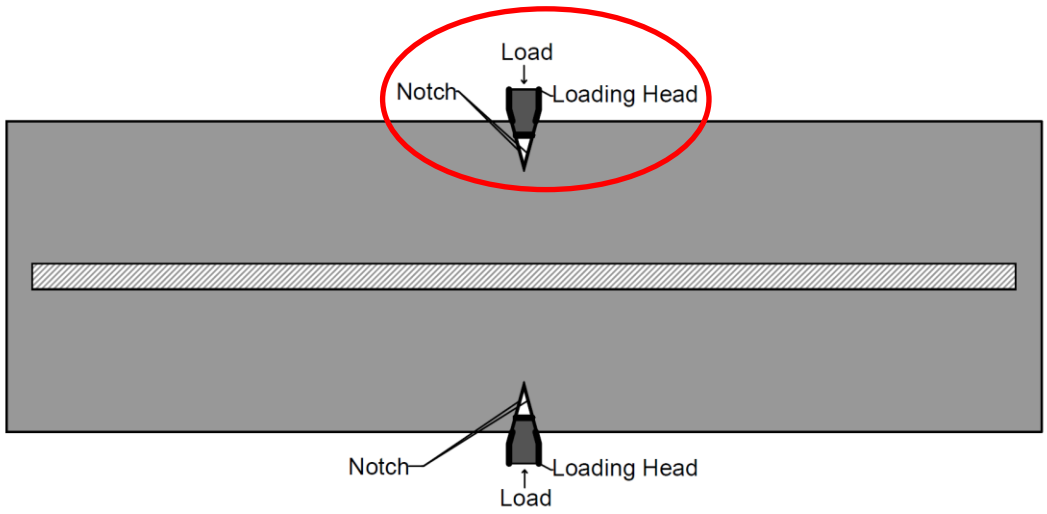

(A)

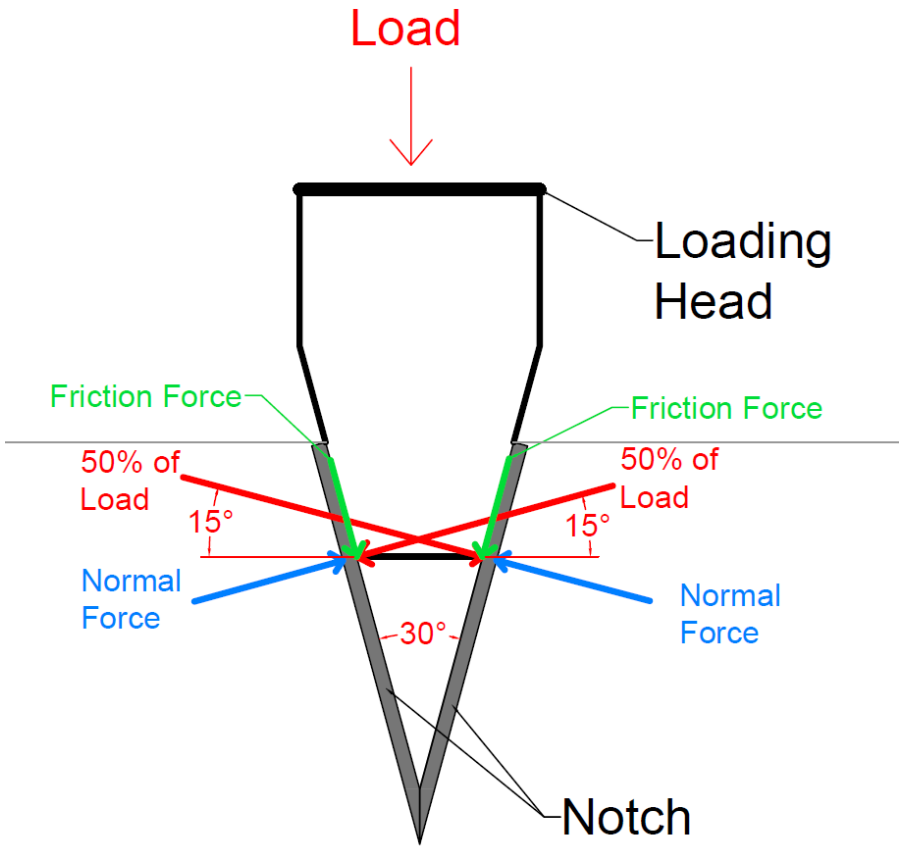

Figure I- 6:(A) Schematic of the beam
(B) Free body diagram of top notch shown in red circle in (A)

Load: The Instron applies a vertical load through the loading head which is applied at an angle of 15° with respect to x-axis, on both faces of the notch. The total vertical load is divided equally between the faces of the notch as shown in red text.

Normal force (N): The load is resisted by an equal and opposite normal force by the concrete beam as shown in the blue text.

Friction force ($\mu_s N$): Since the loading head moves against the notch, a friction force is generated by this contact shown in green text. This friction force acts parallel to the surface of the notch and resists the motion of the loading head against the notches. Since both the contact surfaces are made up of steel, a static friction coefficient (μ_s) should be applied ranging from 0.5 to 0.8

(Engineering ToolBox 2004). For this work, the lower limit of friction coefficient i.e. 0.5 is assumed as the both the steel surfaces are clean and dry.

The components in the x-axis direction are taken from the free-body diagram and the tensile force is calculated as shown below.

The average 3-day compressive strength (f'_c) test results were obtained from another graduate student at Oklahoma State University, Michael Dickey who was using the same mix design as in this chapter. It was performed in accordance with (ASTM C39 2015) and gave an average value of 4133 psi (Values courtesy of Michael Dickey, OSU). From the compressive strength, the direct tensile strength and the modulus of elasticity is calculated using ACI 318-19 building code (American Concrete Institute 2019).

Modulus of Elasticity: $E_c = 57{,}000\sqrt{f'_c}\,(in\ psi)$ (ACI 318-19 Eq. 19.2.2.1b)

Direct tensile Strength: $f_t = 4\sqrt{(f'_c)}\,(in\ psi)$ (ACI 318-19 R22.7.5)

The modulus of elasticity of steel is taken as 29,000,000 psi. The depth of the beam at the point where the load is applied is calculated by subtracting the top and bottom notches from the total depth of 6 inch [*152 mm*].

The detailed calculations for the whole beam with an applied load of 1000 lbs. at which the concrete is not cracked, are shown below.

Total horizontal friction force ($\mu_s N$) = 0.5*517.6 = 259 lbs.

Total horizontal normal force = 2*0.966*1000 = 1932 lbs.

Effective horizontal force = 1932 – 259 = 1673 lbs.

Modulus of elasticity of concrete (E_c) = 3,664,439 psi

Modulus of elasticity of steel (E_s) = 29,000,000 psi

Depth of beam at load point = 6 – 2*0.966 = 4.1 in

Cross-sectional area of concrete (A_c) = 6 in*4.1 in = 24.6 in^2

Nominal area of steel (#4 bar) (A_s) = 0.2 in^2

Direct tensile strength of concrete = 257 psi

E_c*A_c = 3,664,439*24.6 = 90,145,199 kip

E_s*A_s = 0.2*29,000,000 = 5,800,000 kip

Percentage of force in steel = 6%

Percentage of force in concrete = 94%

Stress in steel = (1673*0.06)/0.2 = 502 psi

Stress in concrete = (1673*0.94)/24.6 = 64 psi

1.3 Results and Discussion

1.3.1 Reduction in crack size after unloading

When the beam is unloaded, the crack size reduces, and the percentage of reduction is shown in Figure I- 7. Since the crack size reduces after unloading but does not close completely, it can be assumed that either the steel has some plastic deformation or the bond between concrete and steel has been damaged or it is a combination of both. The linear trendline shows that as the initial crack size increases, the reduction in size after unloading decreases and therefore, it can be deduced that the damage to the bond or the plastic deformation in steel or both, increase as the initial crack size increases. However, there is not a strong correlation for this trend as some larger cracks exhibit a similar reduction as some smaller cracks.

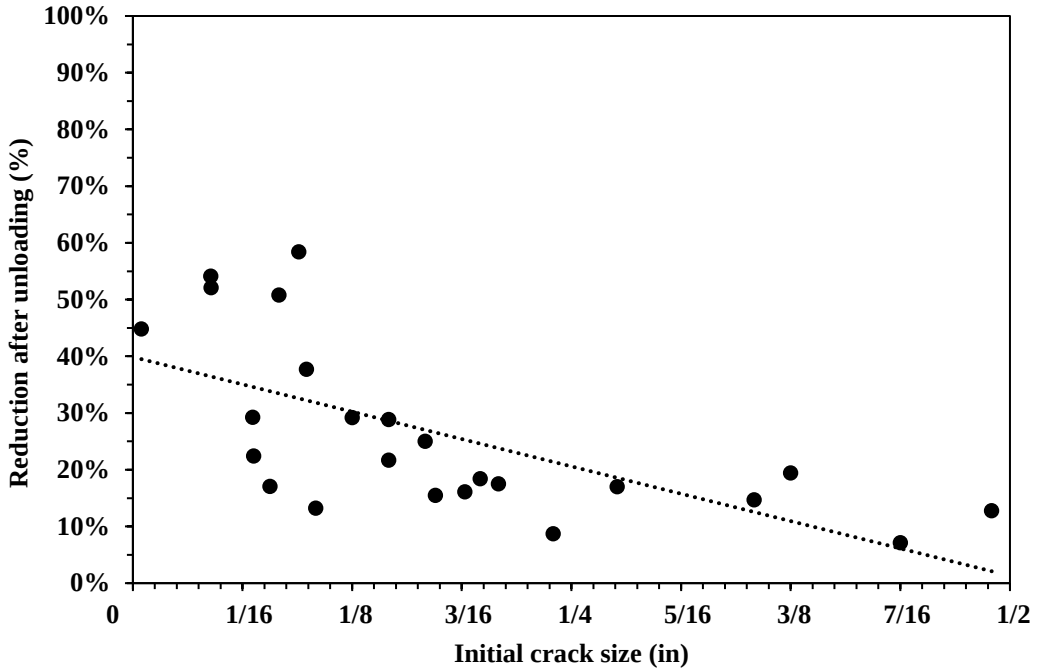

Figure I- 7: Reduction in crack size (%) after unloading compared to initial crack size [1 inch = 25.4 mm]

1.3.2 Comparison of stress at first crack to direct tensile strength

The mean of the load for all beams at which the first crack occurred is 3739 lbs. The mode and the median are 3500 lbs. The coefficient of variance is 17% and the sample standard deviation is 626 lbs.

Just before the crack occurs, the stresses are:

Stress in steel = 1877 psi

Stress in concrete = 239 psi

After the concrete cracks, all the load is resisted by the steel. After the crack, the stress in steel is:

Stress in steel = 31,277 psi

The tensile stress when the concrete cracks is 239 psi which is 7% less than the direct tensile strength estimated from the ACI 318-19 building code. This slight difference may be due to the actual friction conditions that are not accurately represented by the friction coefficient.

1.4 How to create known crack sizes

The objective of this chapter is to create known crack sizes consistently. For that, a simple procedure is developed which is explained below.

Figure I- 8 shows the final crack size on the y-axis and the initial crack size on the x-axis. There is a total of 24 data points where each point represents one beam and is obtained by taking the mean value of six measurements of that beam. Two beams are not included as they were mishandled while unloading therefore affecting the final crack size due to impact. A linear trendline is also shown along with the equation and R squared value.

Using this equation/plot, the initial crack size can be determined for a desired final crack size.

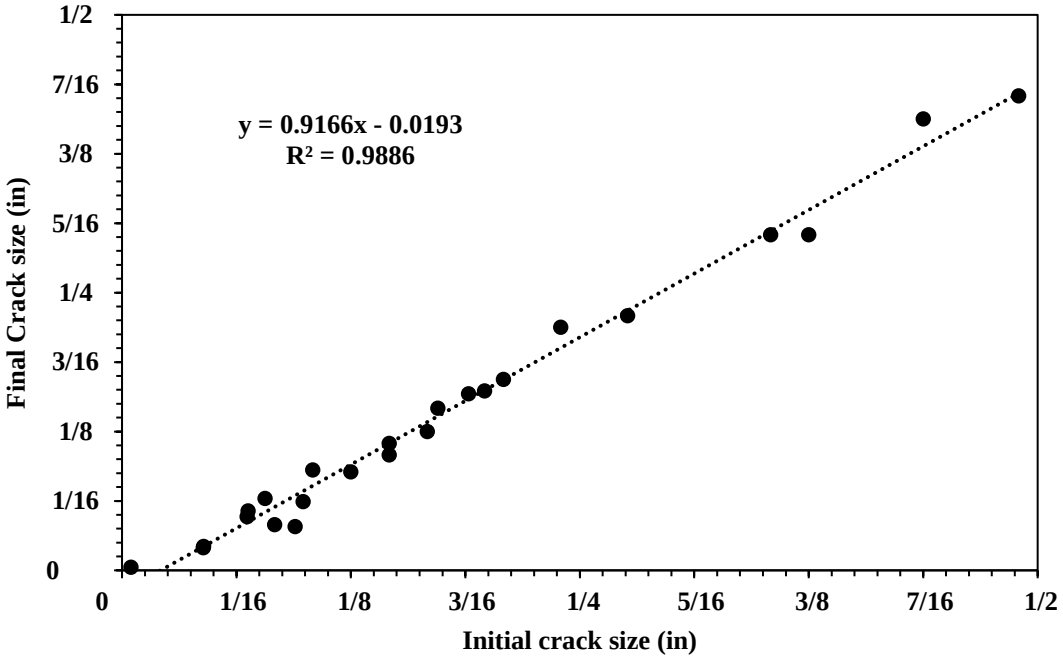

Figure I- 8: Initial crack size vs. final crack size for all beams [1/16 in = 1.59mm]

The plot shown in Figure I- 9 has displacement on the y-axis and on the x-axis, the crack size is plotted which is the mean value of 6 measurements for a single loading interval of 500 lbs. There is a total of 260 data points where each point is obtained by plotting the displacement against the respective crack size for all beams. A linear trendline is also shown along with the equation and the R squared value. Using this plot, the displacement that is required to produce an initial crack size calculated from Figure I- 8, is determined. When the Instron reaches this displacement, the test is stopped.

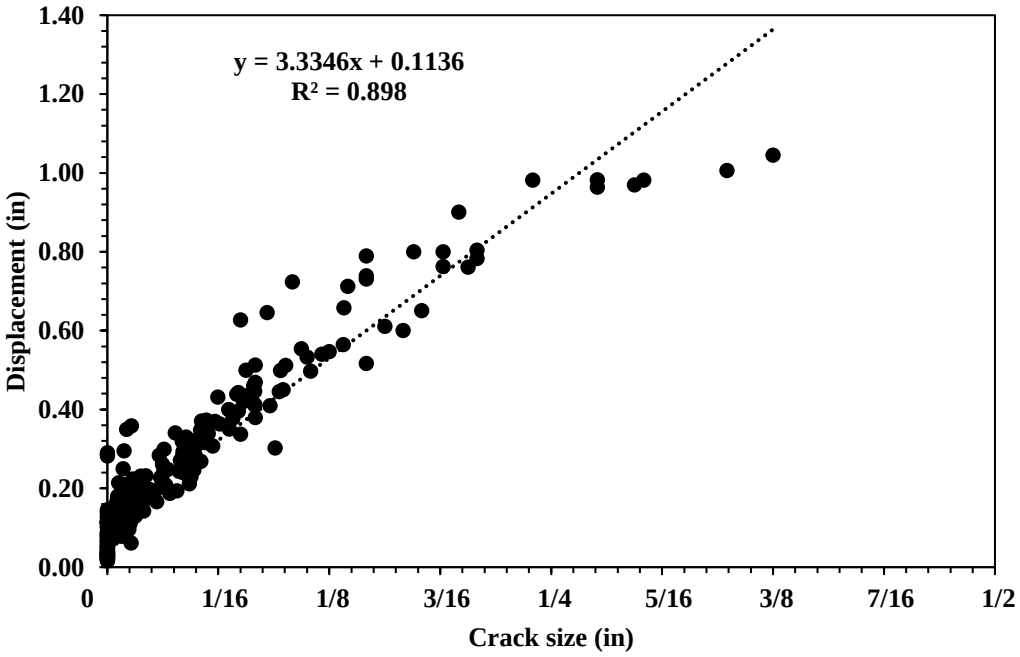

Figure I- 9: Crack size vs. displacement for all beams [1/16 in = 1.59mm]

The plot shown in Figure I- 10 has displacement on y-axis and the final crack sizes on x-axis. There is a total of 24 data points where each point represents one beam and is obtained by plotting the final crack size of that beam against the respective displacement. This plot can also be used to create known cracks sizes by calculating the displacement against the desired crack size.

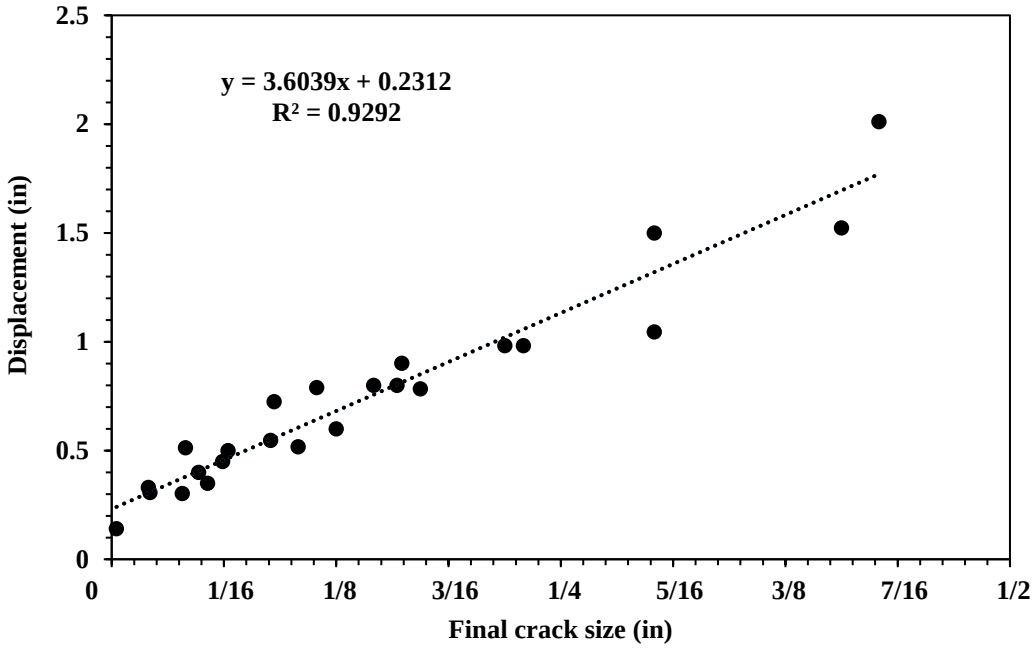

Figure I- 10: Final crack size vs. displacement for all beams [1/16 in = 1.59mm]

To summarize, the following steps can be followed to create a known crack size:

1. Determine the final crack size that is required.
2. Use the plot/equation in Figure I- 8 to determine the initial crack size.
3. Use the plot/equation in Figure I- 9 to determine the displacement.
4. Program the Instron to stop at the displacement determined in step 3.
5. Unload the beam and measure the final crack size.

The above-mentioned methodology was applied to create a known crack size in two beams. First, a desired final crack size was chosen randomly. Then, using plots in Figure I- 8 and Figure I- 9, the initial crack size and the displacement was calculated respectively. The calculated displacement was then used as the ending parameter in the Instron to stop the test. The beam was tested according to the methodology outlined in Figure I- 4. At the end, the final crack size was measured using a crack card. The detailed calculations are shown in Table I- 2.

Table I- 2: Calculations for 2 trial beams

Description	Beam 1	Beam 2
Desired final crack size	0.0625 inch (1/16 inch) *1.59 mm*	0.0400 inch (0.64/16 inch) *1 mm*
Calculated initial crack size from Figure I- 8	0.0892 (≈1.4/16 inch) *2.27 mm*	0.0647 inch (≈1/16 inch) *1.64 mm*
Measured initial crack size using crack card	0.0990 inch (≈1.4/16 inch) *2.51 mm*	0.0688 inch (≈1/16 inch) *1.75 mm*
Calculated displacement from Figure I- 9	0.4442 inch *11.3 mm*	0.3495 inch *8.9 mm*
Displacement set on Instron as ending parameter	0.4500 inch *11.4 mm*	0.3500 inch *8.9 mm*
Final crack size (measured with crack card)	0.0617 inch (≈0.9/16 in) *1.57 mm*	0.0533 in (≈0.85/16 in) *1.35 mm*

For the two beams, the initial crack size that was produced during testing was slightly higher than what was calculated using Figure I- 8. The final crack size obtained from testing was very close for Beam 1 and higher for Beam 2 compared to the calculated final crack size.

Based on these two trials, the results were as expected but a sufficient validation is still required, and the author recommends more samples be tested.

1.5 Conclusions

This work establishes a simple technique to create known crack sizes in reinforced concrete beams using a simple experimental setup. It is found that:

- The crack sizes decrease upon unloading but do not close completely which shows that either the steel has some plastic deformation or the bond between concrete and steel has been damaged or it is a combination of both.
- As the initial crack size increases, the reduction in crack size after unloading decreases which shows that there is an increase in either the plastic deformation in steel or the

damage to the concrete and steel bond or both exhibit an increase at the same time. However, there is not a strong correlation for this trend.

- The tensile stress at the first crack is slightly lower than the direct tensile strength calculated using ACI 318-19 building code.

Crack sizes up to ½ inch were analyzed in this work. Using the steps and plots mentioned in the work, known crack sizes can be created in a consistent manner. This can be very helpful in developing testing procedures to study the effects of crack sizes on various durability mechanisms.

CHAPTER II

PERFORMANCE EVALUATION OF SILANE IN CONCRETE BRIDGE DECKS

2.1 Introduction

One of the major durability issues facing concrete is the penetration of outside chemicals and fluids that cause a host of problems such as corrosion of steel, cracks due to freeze-thaw, and salt scaling (Khanzadeh Moradllo et al. 2015; T. M. Ley et al. 2012). The corrosion of steel reinforcement is primarily caused by exposure to chloride ions from deicing salts and seawater (PCI 2002; Koch et al. 2002; Basham et al. 1995). It is a major cause of deterioration of concrete structures. The penetration of these chemicals depends heavily on the permeability of concrete (Mehta 1991). Permeability is defined by how easy it is for outside chemicals to penetrate the concrete. If the concrete can be made less permeable, the penetration of outside chemicals will decrease which will increase the durability of concrete (Lu et al. 2006; Dean et al. 2009).

To prevent the mass transport of outside fluids, one strategy is to use surface treatments that are applied on the exposed surface of concrete and they decrease the ingress of these fluids (Khanzadeh Moradllo, Hu, et al. 2017; Khanzadeh Moradllo et al. 2016). Generally, these treatments are divided into three categories based on their diffusion

characteristics as shown in Figure II- 1 (Swamy et al. 1998; Christodoulou et al. 2013; Almusallam et al. 2003). These are:

a) Coatings: These form a protective layer on the surface of the concrete which prevents the transport of liquids and vapors entirely. For maximum effect, these coatings should have adequate engineering properties such as elasticity, thermal stability, crack bridging ability, and fatigue strengths.
b) Reactive sealers: These sealers penetrate and seal the concrete surface pores.
c) Vapor permeable sealers: These sealers react with the concrete surface and form a hydrophobic layer that allows the transport of vapors but prevents the liquids.

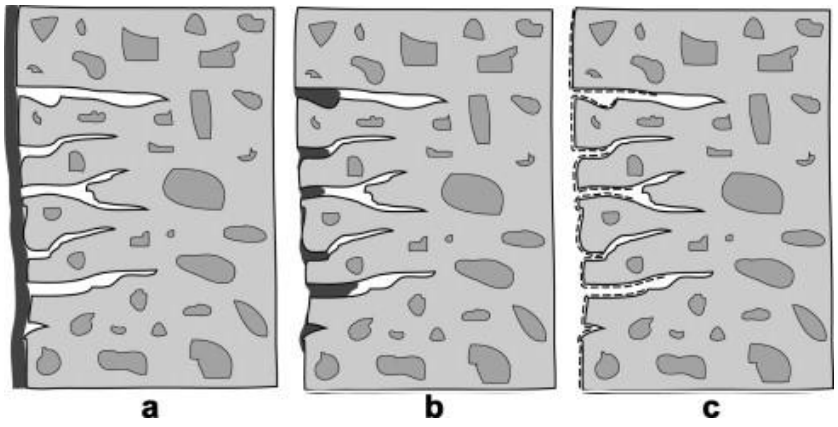

Figure II- 1: Types of surface treatments (a) Coatings (b) Reactive sealers (c) Vapor permeable sealers (Christodoulou et al. 2013)

Silanes are categorized as vapor permeable sealers. They are chemicals containing at least one silicon atom linked to alkyl (CH_3) and alkoxy (CH_3O) groups. The alkoxy groups contain silicon-oxygen bonds that will bond to silicates present in concrete. The alkyl groups has a carbon-silicon bond and they protrude from the pore structure and they are responsible for the hydrophobic characteristics. The basic composition of an alkyl alkoxysilane is shown in Figure II- 2 (Christodoulou et al. 2013).

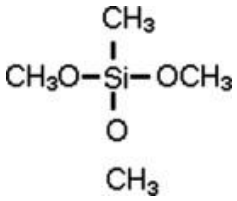

Figure II- 2: Typical alkyl alkoxy silane molecular structure (Christodoulou et al. 2013)

Silanes are generally applied on the concrete surface by dissolving them in a carrier solution. Alcohols are generally used as a carrier and methanol, ethanol, and isopropanol are typical choices. The function of the carrier solution is deeper and uniform penetration into the concrete. The solution containing carrier and silane is applied on the concrete surface by spraying (Witucki 1993). The performance of silanes is greatly affected by the surface imperfections, weather at the time of applications, surface preparations, and skill of the worker (Christodoulou et al. 2013).

Previous research shows that the application of silanes on the concrete surface significantly reduces the ingress of outside chemicals thus reducing the chloride ions penetrations and reducing the corrosion of steel reinforcement (Christodoulou et al. 2013; Ibrahim et al. 1997). As far as the long-term performance of silane is concerned, a study measured the water absorption on concrete bridge decks that were treated with silane 20 years ago. It showed that silane may provide residual protection against ingress of outside chemicals even after 20 years when compared with bridge decks without any silane treatment (Christodoulou et al. 2013). Khanzadeh Moradllo et. al measured the depth of silane penetration in concrete bridge decks that have been in service between 6 and 20 years and found that the silane thickness started to decrease from the bulk of concrete towards the outside after 12 years of service (Khanzadeh Moradllo et al. 2016).

Oklahoma Department of Transportation (ODOT) specifies the use of silane coatings on all the bridge decks with a minimum specified thickness of 1/8 inch [3.2 mm] (Carlisle et al. 2009).

2.1.1 Scope and Methodology

Recently, ODOT reported that silane coatings are not resisting water penetration and the reasons are unknown (ODOT 2019). To investigate this, ODOT sponsored a research project in which 14 samples from 14 concrete bridge decks were provided to Oklahoma State University (OSU) for further investigation of the performance of the silane coatings.

In this study, the depth of penetration of silane and the depth of penetration of outside chemicals inside the concrete surface was measured. The depth of silane is measured using optical staining techniques and Transmission X-ray microscopy (TXM) was used to measure the depth of penetration of outside chemicals into the concrete surface.

2.2 Experimental Methods

2.2.1 Sample acquisition and mixture design

14 cylindrical samples from 14 bridge decks were provided by ODOT each with a diameter of 4 inch [*100 mm*] and variable lengths. After construction, silane was applied on the bridge decks within a year. The mix design was available for 10 samples only as listed in Table II- 1. The minimum water to cementitious ratio for all mix designs is 0.41, a minimum cementitious content of 564 lb/yd^3 [*334 kg/m*^{3}] in which Class C fly ash was used at a 20% replacement rate in some of the mix designs.

Table II- 1: Mix design of all the 14 samples

Sample	Coarse Aggregate			Fine Aggregate		Cement	Air content %	Fly Ash			Water lb/yd^3 *kg/m^3*	Water Reducer (ASTM C-494 Type A/D)			Air-entrainer (ASTM C-260)		w/cm ratio
	Name	Specific Gravity	lb/yd^3 *kg/m^3*	Specific Gravity	lb/yd^3 *kg/m^3*	lb/yd^3 *kg/m^3*		Type	Specific Gravity	lb/yd^3 *kg/m^3*		Type	Specific Gravity	lb/yd^3 *kg/m^3*	Specific Gravity	lb/yd^3 *kg/m^3*	
1	#67	2.69	1850 *1098*	2.62	1232 *731*	564 *335*	6	NONE			250 *148*	A35	1.01	1.5 *0.89*	1.00	0.3 *0.18*	0.44
2	#67	2.69	1800 *1068*	2.62	1195 *709*	611 *362*	6	NONE			267 *158*	A36	1.01	3.2 *1.9*	1.00	0.1 *0.06*	0.44
3	#67	2.69	1840 *1091*	2.62	1230 *730*	452 *268*	6	C	2.65	112 *66*	248 *147*	A37	1.01	1.9 *1.1*	1.00	0.1 *0.06*	0.44
4	#67	2.69	1810 *1074*	2.62	1210 *718*	489 *290*	6	C	2.65	122 *72*	250 *148*	A38	1.01	2.4 *1.4*	1.00	0.2 *0.12*	0.41
5	**Not Provided**																
6																	
7																	
8																	
9	#67	2.67	1800 *1068*	2.62	1195 *709*	611 *362*	6	NONE			267 *158*	A36	1.01	3.2 *1.9*	1.00	0.1 *0.06*	0.44
10	#67	2.67	1807 *1072*	2.62	1204 *714*	489 *290*	6	C	2.65	122 *72*	250 *148*	A38	1.01	2.4 *1.4*	1.00	0.2 *0.12*	0.41
11	#57	2.65	1700 *1009*	2.63	1310 *777*	451 *268*	6.5% ± 1.5%	C	2.65	113 *66*	250 *148*	A35	**Not Provided**		**Not Provided**		0.44
12	#57	2.65	1700 *1009*	2.63	1310 *777*	451 *268*	6.5% ± 1.5%	C	2.65	113 *66*	250 *148*	A35					0.44
13	#57	2.65	1720 *1020*	2.63	1310 *777*	564 *335*	6.5% ± 1.5%	NONE			250 *148*	A36					0.44
14	#57	2.65	1720 *1020*	2.63	1310 *777*	564 *335*	6.5% ± 1.5%	NONE			250 *148*	A37					0.44

2.2.2 Depth of penetration of silane

The depth of the silane layer present was measured using a very simple optical staining technique as used by Khanzadeh et. al (2016). It was shown that the depth of silane penetration can be effectively measured by staining the concrete surface with a blue clothes dye which changes the color of concrete where silane is not present and the portion where silane is present remains the same (Khanzadeh Moradllo et al. 2016).

The sides of all the samples were polished at 9 different spots for 5 minutes with 120-grit sandpaper to remove any laitance and to expose a fresh surface of concrete shown in Figure II- 3.

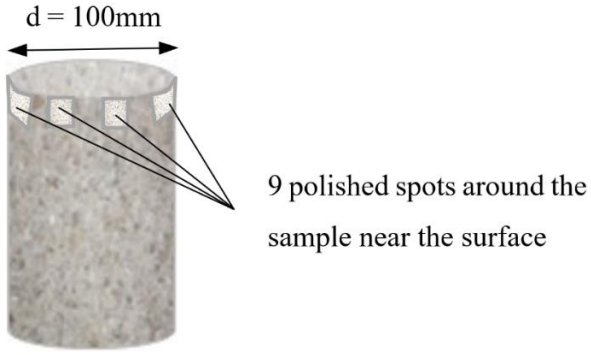

Figure II- 3: Polished spots near the surface of a typical sample to measure the silane penetration depth

The 9 polished spots of all the samples were stained with a dye and after the dye had dried, images were taken using a digital microscope. The silane profile was marked by visual observation of the images depending on the color change of dye. For each polished spot, 5 measurements of the depth of silane were taken at regular intervals using an imaging software. Since there are 9 polished spots and 5 measurements per spot, that gave a total of 45 measurements for each sample. The silane penetration depth was calculated by taking the mean value of the 45 measurements for each sample. Then the standard deviation was calculated on 45 measurements of each individual sample. A typical silane profile for one of the nine polished spots marked visually is shown in Figure II- 4.

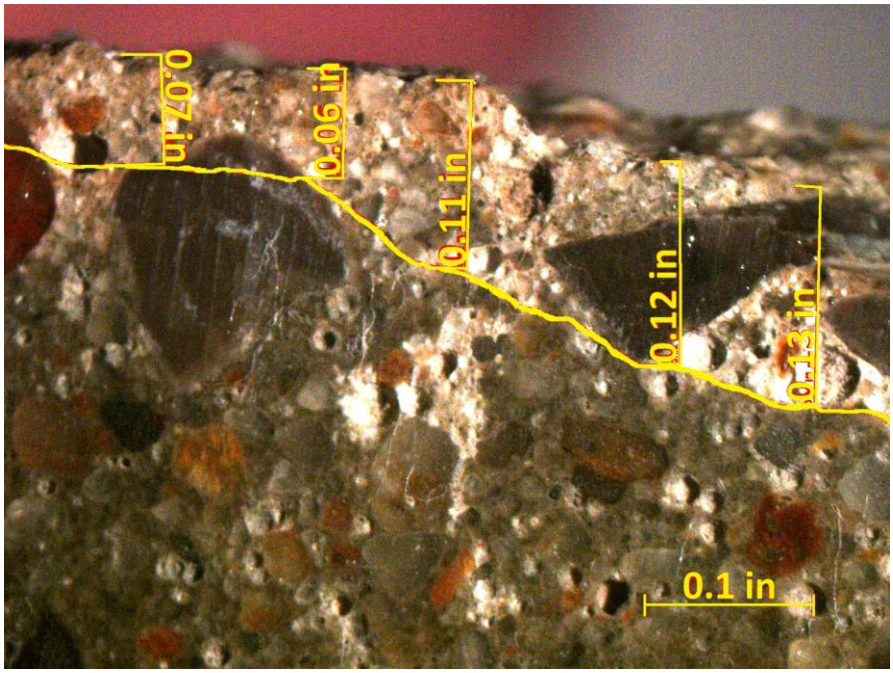

Figure II- 4: Silane coating profile for one polished spot marked visually under a digital microscope [1 inch = 25.4mm]

2.2.3 Depth of penetration of outside chemicals

The penetration of outside chemicals into the concrete matrix was measured using transmission x-ray microscopy (TXM) technique as used by Khanzadeh et. al (2017). X-Ray imaging techniques are rapid, convenient, and non-destructive methods to accurately measure the depth of penetration of outside chemicals into the concrete surface (Lu et al. 2006; Dean et al. 2009). It was shown that the ingress of outside fluids into the concrete can be visualized and quantified effectively using the TXM technique which is explained below (Khanzadeh Moradllo, Hu, et al. 2017).

2.2.3.1 Sample preparation

From each of the 14 samples, 4 smaller cores of ¾ inch [19 mm] diameter were extracted; 2 cores from the top with the silane and 2 cores from the side without silane. An overview is shown in Figure II- 5(A). These cores were also inspected to make sure that they did not contain a large aggregate near their surface as this would interfere with the diffusion measurement. If this occurred, then another core was taken. Next, the cores were oven-dried at 50°C until a state of

mass equilibrium was reached at which less than 0.03% weight change occurred in 24 hours. That mass equilibrium was reached in 5 days. After this, the Degree of Saturation (DoS) of the cores was recorded which was 2.05±0.48 %. Then the sides of the cores except the surface were coated with a hydrophobic wax to force the outside fluid to penetrate in only one direction from the unwaxed top as shown in Figure II- 5(B). After waxing, a PVC hexagonal nut was attached to the bottom of the samples. This nut was matched with the hexagonal stage of the x-ray machine to load the samples in a consistent manner in the machine.

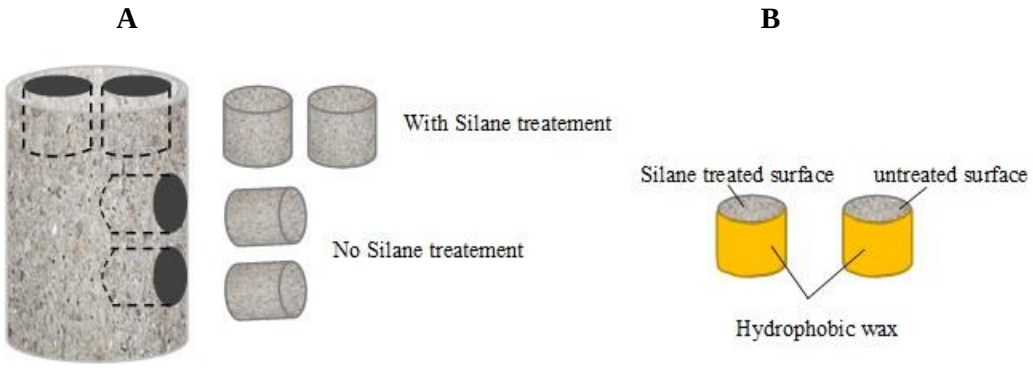

Figure II- 5: (A) Extraction of ¾ inch [19mm] diameter cores from each sample (B) Application of wax on sides and bottom of each core

2.2.3.2 Transmission X-ray Microscopy (TXM)

Skyscan 1172 μCT scanner with the setting summarized in Table II- 2 was used to conduct the experiments and take radiographs at the desired intervals.

Table II- 2: Settings used in TXM technique

Parameter	TXM setting
Pixel Size (mm)	8.8
Voltage (Kev)	100
Current (mA)	100
Filter	0.5 mm Al +Cu
Acquisition Time	8 s
Chamber Condition	Air

In this machine, each core was loaded on a fixed stage between the x-ray source and the detector. When x-rays hit the loaded core, some parts of the x-rays are absorbed by the core and some pass the core unabsorbed to reach the detector. The detector produces simple grayscale radiographs based on the received x-rays as shown in Figure II- 6.

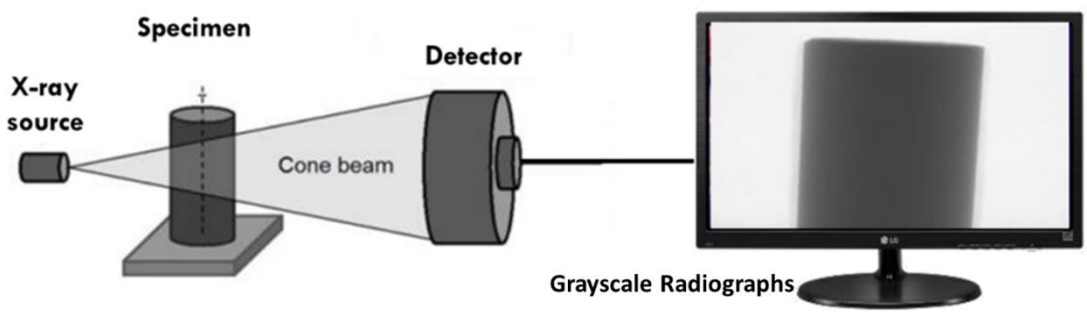

Figure II- 6: Schematic of X-ray imaging process

Each pixel in the taken radiographs has a gray value between "0" which represents pure black to "255" which represents pure white. Values in between make up the different shades of gray as shown in Figure II- 7. In the captured radiographs, materials with a higher density are darker (have low gray values) and materials with low density are brighter (have high gray values). When a solution with high electron density penetrates a core, the penetrated depths get lower gray values and consequently become darker because of the free, absorbed and bound ions.

Figure II- 7: Correlation of gray scale values, brightness, and density

An initial radiograph was taken before ponding the core with the solution. To check the gray value change at different depths in this method, secondary radiographs of each individual core taken at different days after ponding with solution are compared to the corresponding initial

radiograph. The concept behind this technique is that when a solution with high electron density penetrates a core, the penetrated depths in the secondary radiographs look darker in comparison to the initial radiograph as shown in Figure II- 8. By adopting a quantitative approach, concentration profiles and penetration depth of the solution can be extracted from the comparison of initial radiograph with the secondary radiograph using calibration curves.

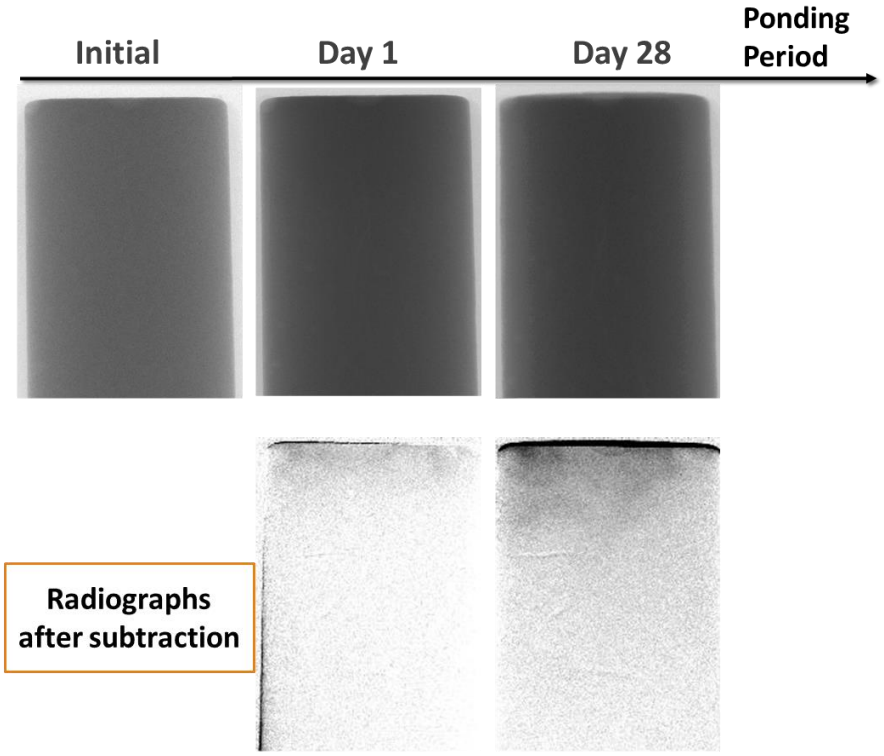

Figure II- 8: Radiograph at different time periods after initial is subtracted

The diffusion test in this study uses a tracer salt solution on top of the unwaxed surface of the cores to study the one-directional mass transport into the cores for 28 days. In this test, the gravity and moisture movement in the cores are in the same direction. In this technique, the initial radiographs taken from the cores before ponding the solution are compared with the correlated secondary radiographs taken from the same cores at subsequent time intervals after starting the experiment.

Since the applied x-ray microscopy technique can capture materials with high electron density, potassium iodide (KI) was chosen to be used as the tracer because iodine strongly absorbs x-ray waves due to its high electron density (Khanzadeh Moradllo, Hu, et al. 2017; Khanzadeh Moradllo and Ley 2017; M. T. Ley et al. 2017). Furthermore, iodide and chloride ions are similar in size (iodide radius is 206 pm versus a chloride radius of 167 pm) which can provide valuable insights into the chloride diffusion mechanism of cement-based materials (Khanzadeh Moradllo, Hu, et al. 2017). The concentration of the KI solution was chosen equal to 0.6 mol/L to get enough contrast between the core and the solution in the radiograph images. This matches previous procedures used to study the diffusion coefficient of concrete (Khanzadeh Moradllo, Hu, et al. 2017).

Each smaller core was scanned from two different directions. First, the core was scanned in one direction, then it was rotated 90 degrees and scanned in that direction. To compare the radiographs of each individual core, all the radiographs taken at other time intervals should be identical to its initial radiograph. For taking consistent radiographs at different time intervals for each individual core, it is necessary to scan the cores in a consistent manner over time so that it is scanned in the exact same position every time. For this purpose, an appropriate stage was designed to fix the position of the cores in the X-ray scanner. This stage forces to load the core in a consistent and fixed manner and scan each side of the core in the same exact position as the initial radiograph without any positional error at each time interval. Keeping the direction constant becomes more important when concrete samples are being investigated.

To start the diffusion test, cores were transferred to separate cells and a 0.6 mol/L KI solution was used to fill the empty space between the cores and the cells walls to reach above the unwaxed surface of the cores up to 2 mm. The salt solution was kept on the cores for 28 days. In this period, the KI solution was changed every five days to keep the concentration constant. During the experiment, the cells were covered to prevent any evaporation and change in the solution

concentration. All cores were kept at room temperature (23 ºC) during the experiment. The cores were scanned at several time periods up to 28 days after ponding to get the secondary radiographs. Results represented are extracted from radiographs taken after 28 days of ponding.

2.2.3.3 Data Analysis

To analyze and compare the taken radiographs, a software programming code with minimal user intervention was prepared to apply local displacements on each image and align the secondary radiographs with the reference radiograph of each individual core. Then, the central region of the cores with an approximate width of 100 pixels (0.88 mm) was considered to get the average of gray values at each depth interval for each core as shown in Figure II- 9. The center region was considered to eliminate cupping artifact which refers to a locally bright appearance along the periphery of a sample. Because the tested samples had a cylindrical shape, the center of the sample appears denser than the regions near the sides if viewed from a fixed direction. For this reason, the x-ray beam is "hardened" by passing through the center region of the sample and the mean photon energy will be higher around the center. Since higher energy photons are less attenuated by the denser region, the beam will be less attenuated versus identical material near the sides. The obtained gray value profiles for each time series radiographs were subtracted from the gray value profile obtained from the reference images to quantify the changes in gray values because of mass transport in the samples. The Beer-Lambert Law (Eq. (1)) was used to turn the subtracted gray values in attenuation at different depths of each core (Tidwell et al. 2000; Cavé et al. 2009).

$$(\Delta\mu)_x = \ln (I_{ref}) - \ln (I_t)_x \qquad (1)$$

where $(I_{ref})_x$ is the transmitted X-ray intensity (gray value) at depth x on the reference profile and $(I_t)_x$ is the transmitted X-ray intensity at the same depth at other intervals.

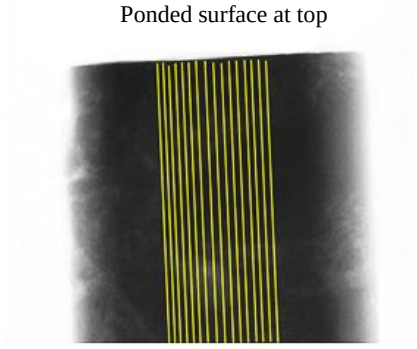

Figure II- 9: Considered region for data analyzing in each radiograph

To convert the calculated attenuations to concentration, calibration curves were applied. Calibration curves are those graphs that plot concentration vs. attenuation. To develop the calibration curves, standard samples made with known iodide concentration added to the mixtures during mixing were used. These standard samples were scanned with the setup provided in Table II- 2. After scanning the standard samples, the attenuation correlated to each concentration was calculated. Ultimately, a curve was fitted on the obtained spots to get an equation that converts the attenuation to the concentration. By using the obtained equation, concentration profiles correlating to different duration of ponding were plotted for each core. In these profiles, the ion concentration in terms of weight percentage of the paste is calculated and plotted against the depth. The obtained concentration profiles give information about the concentration at each depth and the slope of the profiles gives an idea about the rate of penetration. As a profile follows a flatter slope, it implies having a higher rate of mass transport.

2.3 Results and Discussion

2.3.1 Depth of silane penetration

The silane penetration depth of all the 14 projects was measured using the testing regime described in section 2.2. The mean depth for each sample is shown in Figure II- 10 along with error bars showing one standard deviation. The mean value of the 14 samples was found to be approximately 2.5 mm which is less than the minimum specified depth of 3.2 mm by ODOT.

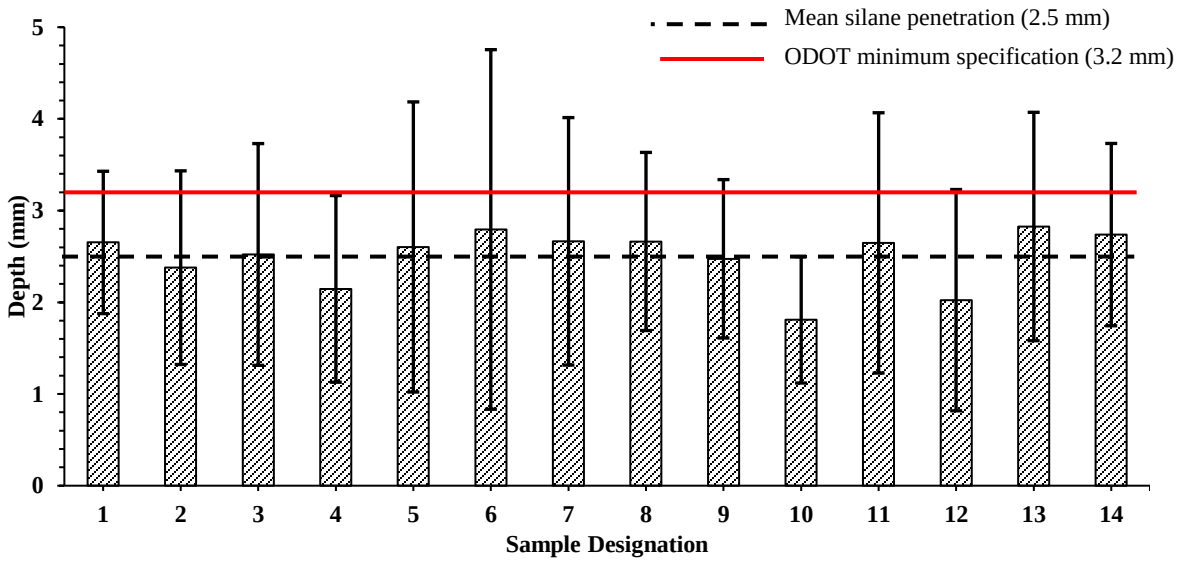

Figure II- 10: Average depth of silane penetration for all samples

2.3.2 Performance of silane coating

An iodide concentration profile for sample 3 is shown in Figure II- 11. The dashed line represents the data of the smaller cores taken from the side without any silane treatment and the solid lines show the data for the silane treated smaller cores taken from the top of the sample. Each silane (solid line) and non-silane (dashed line) is an average of four concentration profiles; two smaller cores are imaged from two directions resulting in a total of four profiles for silane cores and in a similar manner, four profiles for non-silane cores. All the iodide concentrations are calculated as a percentage of the weight of the paste content.

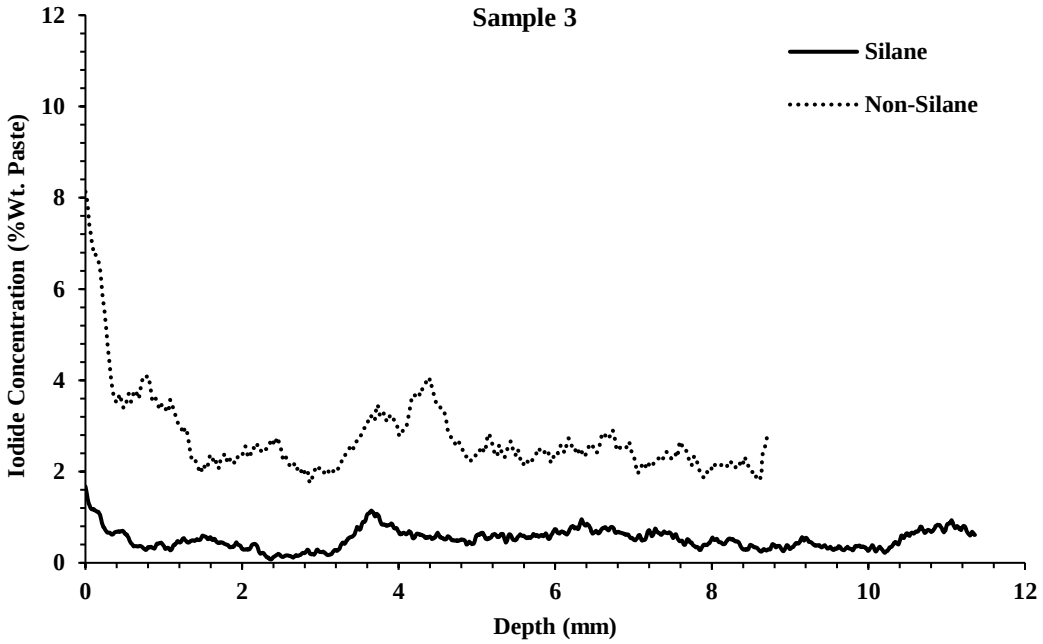

Figure II- 11: Iodide concentration profile of sample 3

The iodide concentration profiles of all silane treated samples collected from 14 locations are shown in Figure II- 12. It can be observed that the application of silane decreases the iodide concentration and is effective in keeping the outside chemicals from penetrating. However, in some cases, the concentration values at greater depths for silane and non-silane samples came very close. In some of the samples such as sample 2, it can be observed that the concentration values are low for silane samples near the surface but as the depth increases, the concentration profiles increase and get closer to non-silane samples.

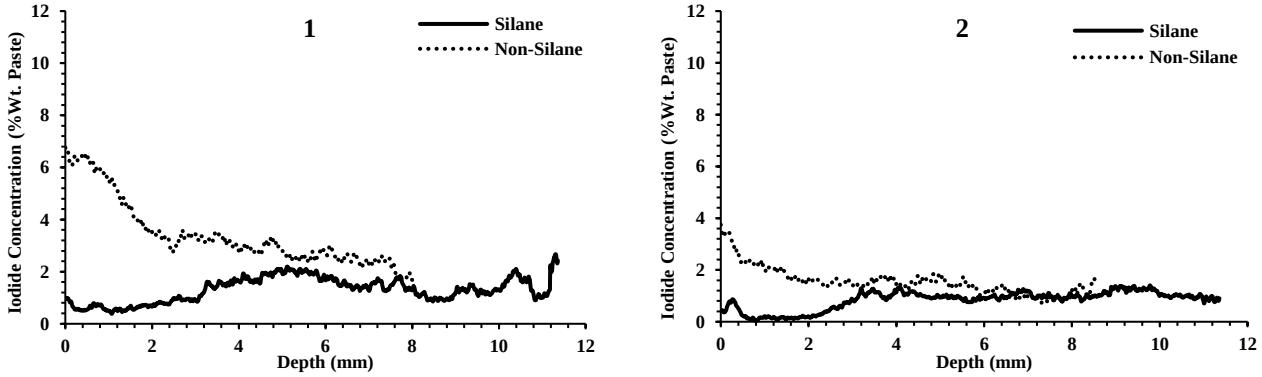

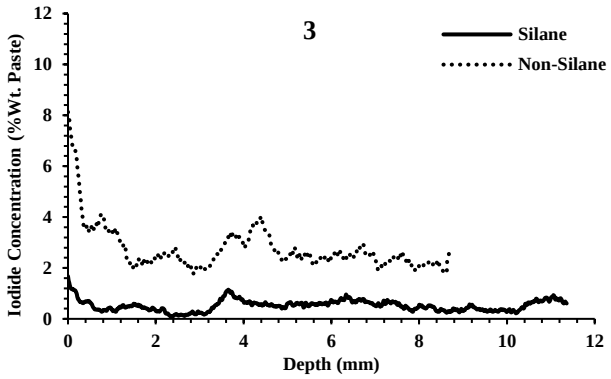
3
Silane
Non-Silane
Iodide Concentration (%Wt. Paste)
Depth (mm)

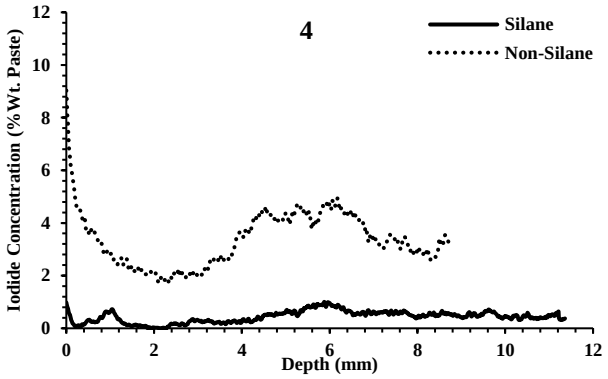
4
Silane
Non-Silane
Iodide Concentration (%Wt. Paste)
Depth (mm)

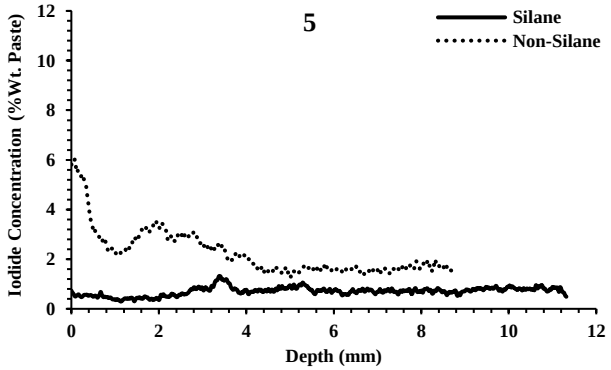
5
Silane
Non-Silane
Iodide Concentration (%Wt. Paste)
Depth (mm)

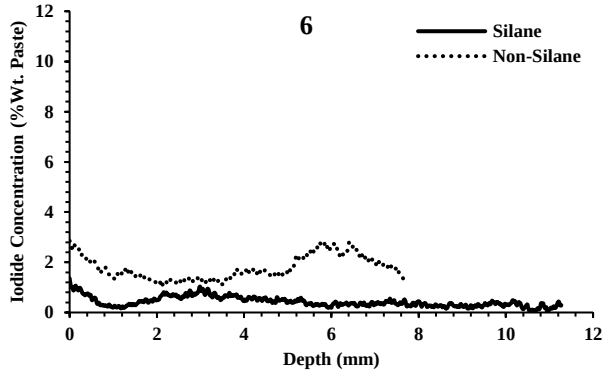
6
Silane
Non-Silane
Iodide Concentration (%Wt. Paste)
Depth (mm)

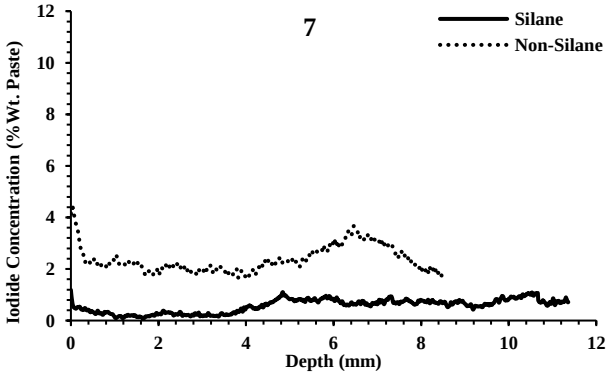
7
Silane
Non-Silane
Iodide Concentration (%Wt. Paste)
Depth (mm)

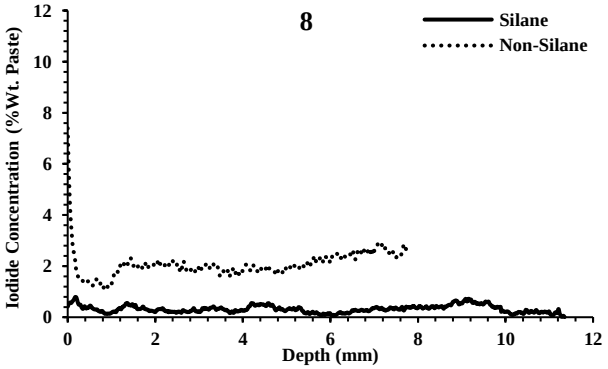
8
Silane
Non-Silane
Iodide Concentration (%Wt. Paste)
Depth (mm)

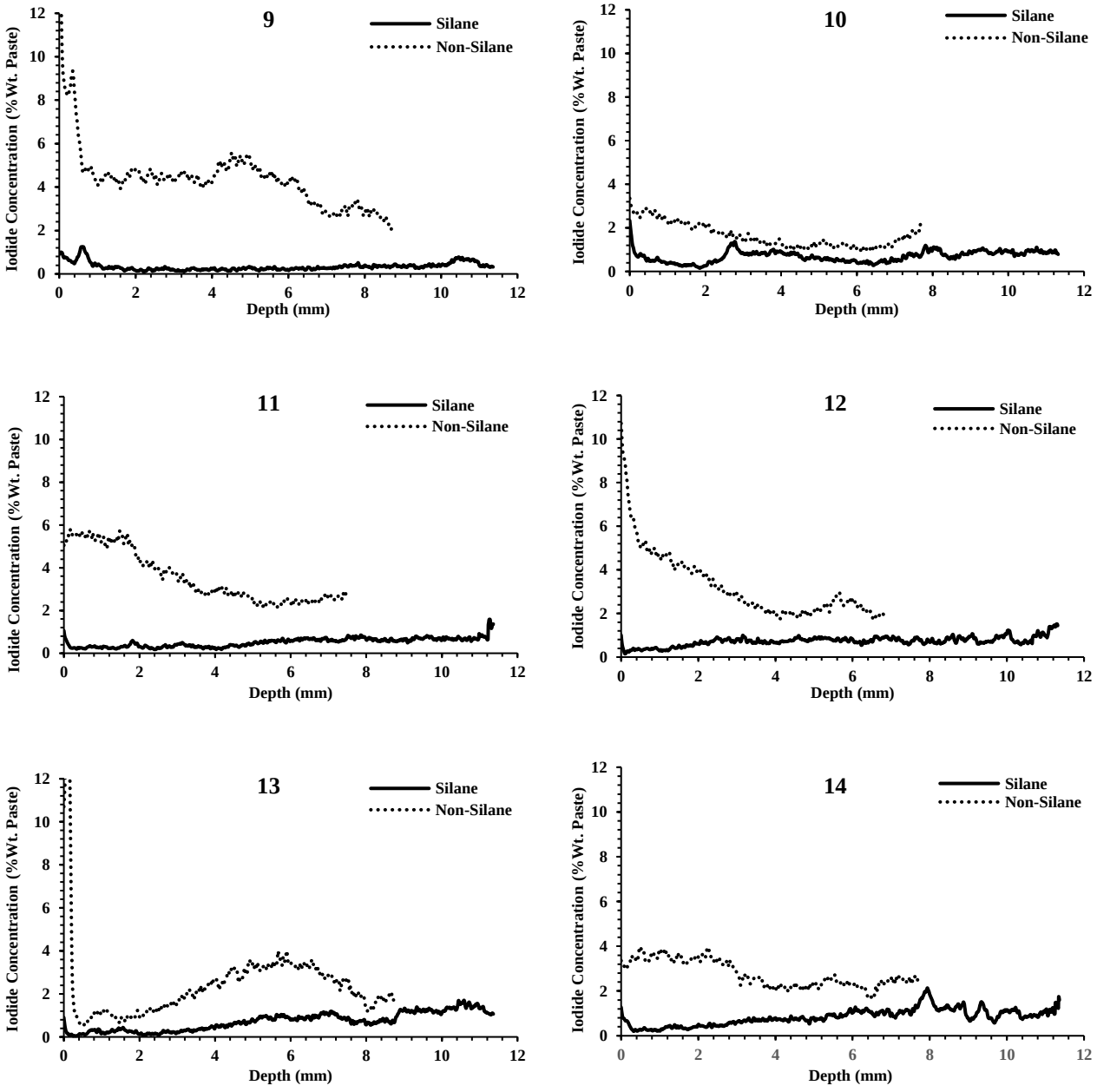

Figure II- 12: Iodide concentration profiles of all samples

To discuss more clearly, the concentration profile of sample 2 shown in Figure II- 13, is discussed. Sample 2 represents the behavior of a defective silane treated sample. In the region shown with the solid green circle, the difference between the silane and non-silane profiles at a depth of 2 mm is very large but at deeper depths shown in the dashed red circle, both

concentration profiles return close concentration values. This means while silane was effective in the first couple millimeters but somehow, the solution could pass the silane coating because of a potential crack in the silane coating or non-uniform performance by the silane.

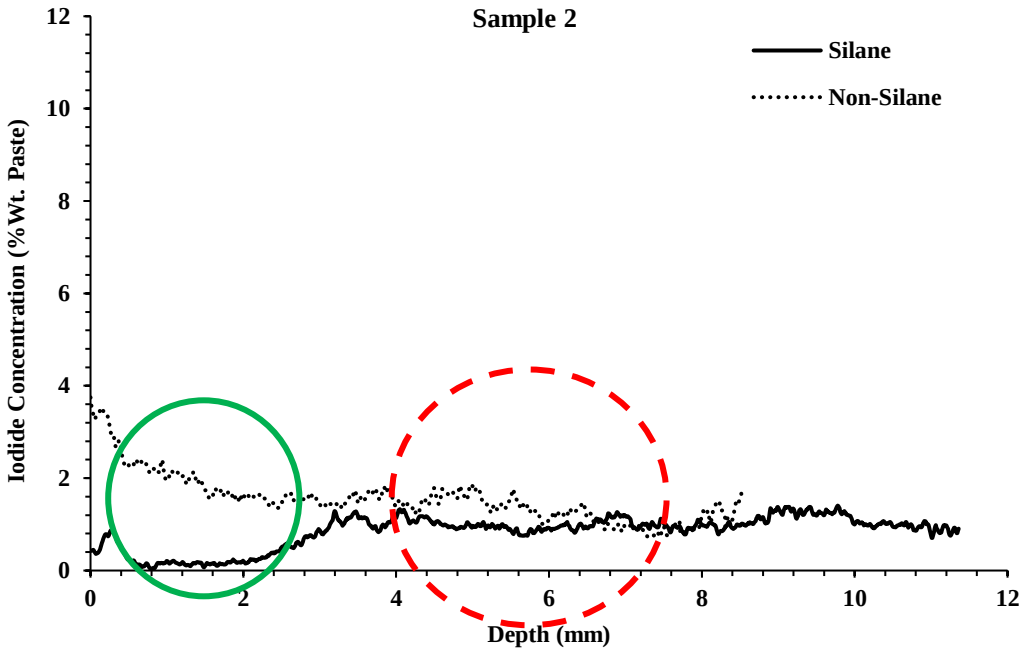

Figure II- 13: Iodide concentration profile of sample 2 with a defected silane coating

Figure II- 14 compares the iodide concentrations of all the samples at a fixed depth of 2 mm for both the silane and non-silane samples. A depth of 2 mm was the maximum plausible depth that silane existed for all the considered samples.

The concentrations in non-silane samples are much higher than silane samples, which suggests that the silane coating is effective in reducing the penetration of outside chemicals. The average of iodide concentration from all non-silane samples at a depth of 2 mm is 2.7% while the average value for silane treated samples at the same depth is 0.3%. Recent discussion interferes that silane limits the harmful ion ingress into concrete by reducing the penetration depth by 8.5 times compared to the non-silane samples.

For the non-silane samples, there exists a large variability among the samples. Some samples have iodide concentrations as low as 1% by weight and some have greater than 4%. This may be caused by the variation in the mixture design and the curing methods employed for these samples.

The range of iodide concentration change for silane treated samples was 0.026% and 0.66%. This shows that the variation of the iodide concentration was low. The possible reason for the observation of low iodide concentration variation is that silane is a surface treatment coating material that acts as a barrier. For this reason, silane performance is not much dependent on the bulk concrete properties. The efficiency of silane is directly dependent on the silane penetration depth into the concrete. The silane penetration depth is dependent on the interconnectedness, tortuosity of the capillary pore structure of the near-surface concrete (Sohawon et al. 2018).

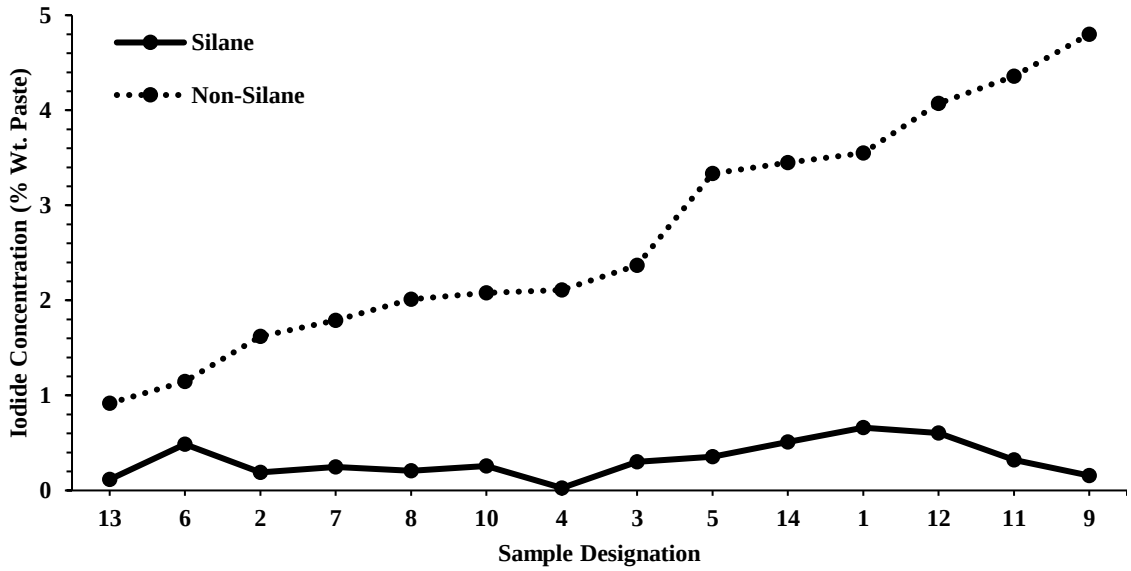

Figure II- 14: Comparison of silane vs. non-silane samples at 2mm depth

2.4 Conclusions

A case study was performed for the samples provided by ODOT, to evaluate the performance of the silane treatments to investigate the inability of silane coatings to resist water penetration. 14 cores from 14 concrete bridge decks treated with silane were investigated using optical staining

and transmission x-ray microscopy to determine the average penetration of silane with visual contrast and the depth of penetration of outside chemicals respectively.

The following observations were concluded from this work:

- The average thickness for the silane coating for the 14 projects is 2.5 mm, which is less than the minimum thickness of 3.2 mm as mentioned in the specifications. Previous research has shown that a 3.2 mm layer of silane will last for 12 years. Since none of the projects in this work meet that thickness threshold, the silane layer may not last as long.
- The silane layers are effective in reducing the iodide concentration by as much as 8.5 times when compared to non-silane samples.
- It was found that > 50% of the samples with silane coating on the surface allowed Iodide to penetrate past the coating. Despite the silane reducing the outside ion penetration, it does not appear that it always stops the outside chemicals.

Some abnormalities like cracks caused silane to lose its efficiency in preventing the outside chemicals enter concrete.

REFERENCES

Abdalla, H. M., and B. L. Karihaloo. 2003. “Determination of Size-Independent Specific Fracture Energy of Concrete from Three-Point Bend and Wedge Splitting Tests.” *Magazine of Concrete Research* 55 (2): 133–41. https://doi.org/10.1680/macr.2003.55.2.133.

Almusallam, A. A., F. M. Khan, S. U. Dulaijan, and O. S.B. Al-Amoudi. 2003. “Effectiveness of Surface Coatings in Improving Concrete Durability.” *Cement and Concrete Composites* 25 (4-5 SPEC): 473–81. https://doi.org/10.1016/S0958-9465(02)00087-2.

American Concrete Institute. 2019. *Building Code Requirements for Structural Concrete (ACI 318-19) Commentary on Building Code Requirements for Structural Concrete (ACI 318R-19)*.

Amirkhanian, A, D Spring, J Roesler, K Park, and G Paulino. n.d. “Disk-Shaped Compact Tension Test for Plain Concrete.”

ASTM C293. 2016. “Standard Test Method for Flexural Strength of Concrete (Using Simple Beam With Center-Point Loading).” *Annual Book of ASTM Standards* 78 (Note 1): 8–10. https://doi.org/10.1520/C0293_C0293M-16.

ASTM C39. 2015. “Compressive Strength of Cylindrical Concrete Specimens.” *ASTM Standards*, 1–7. https://doi.org/10.1520/C0039.

ASTM C78. 2018. “Standard Test Method for Flexural Strength of Concrete (Using Simple Beam with Third-Point Loading).” *Annual Book of ASTM Standards*. https://doi.org/10.1520/C0078_C0078M-18.

ASTM D7313. 2013. “Standard Test Method for Determining Fracture Energy of Asphalt-Aggregate Mixtures Using the Disk-Shaped Compact Tension Geometry.” *Astm International*, 2–8. https://doi.org/10.1016/j.jpag.2008.01.073.

Basham, K, and J Meredith. 1995. “MEASURING WATER PENETRATION.” *Mag. Masonry Constr.* 8 (11): 539–43. https://fabrikem.com/News/WaterPenetration.pdf.

Bordelon, Amanda. 2008. “Manual for Three-Point Bending Single-Edge Notched Fracture Test with Plain or Fiber-Reinforced Concrete.”

Brohwiler, E, and F H Wittmann. 1990. “THE WEDGE SPLITTING TEST, A NEW METHOD OF PERFORMING STABLE FRACTURE MECHANICS TESTS.” *Engineering Fructure Mechanics*. Vol. 35.

Carlisle, Member, Mabrey Iii, Vice-chairman James H Dunegan, Chairman Dan B Overland, Member Jackie R Cooper, Oklahoma City, Member Loyd Benson, et al. 2009. “Oklahoma Department of Transportation Transportation Commission Secretary of Transportation / Director.”

Cavé, L, T Al, Y Xiang, and P Vilks. 2009. “A Technique for Estimating One-Dimensional Diffusion Coefficients in Low-Permeability Sedimentary Rock Using X-Ray Radiography: Comparison with through-Diffusion Measurements.” *Journal of Contaminant Hydrology* 103 (1–2): 1–12. https://doi.org/10.1016/j.jconhyd.2008.08.001.

Christodoulou, C., C. I. Goodier, S. A. Austin, J. Webb, and G. K. Glass. 2013. “Long-Term Performance of Surface Impregnation of Reinforced Concrete Structures with Silane.” *Construction and Building Materials* 48 (November): 708–16. https://doi.org/10.1016/j.conbuildmat.2013.07.038.

Cifuentes, Héctor, Miguel Lozano, Táňa Holušová, Fernando Medina, Stanislav Seitl, and Alfonso Fernández-Canteli. 2017. “Modified Disk-Shaped Compact Tension Test for Measuring Concrete Fracture Properties.” *International Journal of Concrete Structures and Materials* 11 (2): 215–28. https://doi.org/10.1007/s40069-017-0189-4.

Dean, S. W., Gaurav Sant, and Jason Weiss. 2009. “Using X-Ray Absorption to Assess Moisture Movement in Cement-Based Materials.” *Journal of ASTM International*. https://doi.org/10.1520/jai102234.

Engineering ToolBox. 2004. “Friction and Friction Coefficients.” 2004. https://www.engineeringtoolbox.com/friction-coefficients-d_778.html.

Fernández-Canteli, A., L. Castañón, B. Nieto, M. Lozano, T. Holušová, and S. Seitl. 2014. “Determining Fracture Energy Parameters of Concrete from the Modified Compact Tension Test.” *Frattura Ed Integrita Strutturale* 30 (October): 383–93. https://doi.org/10.3221/IGF-ESIS.30.46.

Guan, J F, X Z Hu, C P Xie, Q B Li, and Z M Wu. 2017. “Wedge-Splitting Tests for Tensile Strength and Fracture Toughness of Concrete.” https://doi.org/10.1016/j.tafmec.2017.09.006.

Ibrahim, M., A. S. Al-Gahtani, M. Maslehuddin, and A. A. Almusallam. 1997. “Effectiveness of Concrete Surface Treatment Materials in Reducing Chloride-Induced Reinforcement Corrosion.” *Construction and Building Materials* 11 (7–8): 443–51. https://doi.org/10.1016/s0950-0618(97)87809-9.

Khanzadeh Moradllo, Mehdi, Qinang Hu, and M. Tyler Ley. 2017. “Using X-Ray Imaging to Investigate in-Situ Ion Diffusion in Cementitious Materials.” *Construction and Building Materials* 136 (April): 88–98. https://doi.org/10.1016/j.conbuildmat.2017.01.038.

Khanzadeh Moradllo, Mehdi, and M. Tyler Ley. 2017. “Comparing Ion Diffusion in Alternative Cementitious Materials in Real Time by Using Non-Destructive X-Ray Imaging.” *Cement and Concrete Composites*. https://doi.org/10.1016/j.cemconcomp.2017.05.014.

Khanzadeh Moradllo, Mehdi, Mohammad H. Meshkini, Ehsan Eslamdoost, Seyedhamed Sadati, and Mohammad Shekarchi. 2015. “Effect of Wet Curing Duration on Long-Term Performance of Concrete in Tidal Zone of Marine Environment.” *International Journal of Concrete Structures and Materials*. https://doi.org/10.1007/s40069-015-0118-3.

Khanzadeh Moradllo, Mehdi, Bryan Sudbrink, and M. Tyler Ley. 2016. “Determining the Effective Service Life of Silane Treatments in Concrete Bridge Decks.” *Construction and Building Materials* 116 (May): 121–27. https://doi.org/10.1016/j.conbuildmat.2016.04.132.

Koch, G H, MPH Brongers, N G Thompson, Y P Virmani, and J H Payer. 2002. “CORROSION COST AND PREVENTIVE STRATEGIES IN THE UNITED STATES.” https://trid.trb.org/view/707382.

Ley, M. Tyler, Nicholas F Materer, Bryan Sudbrink, Mehdi Khanzadeh Moradllo, Qinang Hu, M. Tyler Ley, Jeffrey M. Davis, Nicholas F Materer, and Allen Apblett. 2017. “Imaging the Presence of Silane Coatings in Concrete with Micro X-Ray Fluorescence.” *Cement and Concrete Research* 92 (February): 121–27. https://doi.org/10.1016/j.cemconres.2016.11.019.

Ley, Tyler M., Bryan Sudbrink, Harikishan Kotha, Nicholas Materer, and Allen Applett. 2012. “Expected Life of Silane Water Repellant Treatments on Bridge Decks (FHWA-OK-12-08).” https://shareok.org/handle/11244/317845.

Löfgren, Ingemar, Henrik Stang, and John Forbes Olesen. n.d. “WEDGE SPLITTING TEST-A TEST TO DETERMINE FRACTURE PROPERTIES OF FRC.”

Lu, S., E. N. Landis, and D. T. Keane. 2006. “X-Ray Microtomographic Studies of Pore Structure and Permeability in Portland Cement Concrete.” *Materials and Structures/Materiaux et Constructions*. https://doi.org/10.1617/s11527-006-9099-7.

Mehta, P. K. 1991. “Durability of Concrete--Fifty Years of Progress?” *Special Publication* 126 (August): 1–32. https://doi.org/10.14359/1998.

ODOT. 2019. “OKLAHOMA DEPARTMENT OF TRANSPORTATION State Planning and Research Work Program FFY 2020.”

PCI. 2002. “IS536 - Types and Causes of Concrete Deterioration.” *Portland Cement Association*, 1–16. https://www.worldcat.org/title/types-and-causes-of-concrete-deterioration/oclc/52419553.

Sohawon, Haris, and Hans Beushausen. 2018. “The Effect of Hydrophobic (Silane) Treatment on Concrete Durability Characteristics.” In *MATEC Web of Conferences*, 199:07015. EDP Sciences. https://doi.org/10.1051/matecconf/201819907015.

Swamy, R. Narayan, Arvind K. Suryavanshi, and Shin Tanikawa. 1998. “Protective Ability of an Acrylic-Based Surface Coating System against Chloride and Carbonation Penetration into Concrete.” *ACI Materials Journal* 95 (2): 101–12. https://doi.org/10.14359/355.

Tidwell, V C, L C Meigs, T Christian-Frear, and C M Boney. 2000. “Effects of Spatially Heterogeneous Porosity on Matrix Diffusion as Investigated by X-Ray Absorption Imaging.” *Journal of Contaminant Hydrology* 42 (2–4): 285–302. https://doi.org/10.1016/S0169-7722(99)00087-X.

Torkornoo, Selase, Ethan Bradshaw, Stephen R Sharp, and Michael M Sprinkel. 2018. “Design of Artificially Cracked Concrete Specimens for Virginia Department of Transportation Material Evaluation.” http://www.virginiadot.org/vtrc/main/online_reports/pdf/18-r2.pdf.

Wiggenhauser, Herbert, Christian Köpp, Juri Timofeev, and Hoda Azari. 2018. “Controlled

Creating of Cracks in Concrete for Non-Destructive Testing." *Journal of Nondestructive Evaluation* 37 (3): 1–9. https://doi.org/10.1007/s10921-018-0517-x.

Witucki, Gerald. 1993. "A Silane Primer: Chemistry and Applications of AIkoxy Silanes." *Journal of Coatings Technology* 65.

Zhang, Hao, Donghui Fu, Haipeng Song, Yilan Kang, Ganyun Huang, Gang Qi, and Jianyu Li. 2015. "Damage and Fracture Investigation of Three-Point Bending Notched Sandstone Beams by DIC and AE Techniques." *Rock Mechanics and Rock Engineering* 48 (3): 1297–1303. https://doi.org/10.1007/s00603-014-0635-4.

VITA

Syed Muhammad Aqib

Candidate for the Degree of

Master of Science

Thesis: CREATION OF CRACKS OF KNOWN SIZES IN REINFORCED CONCRETE BEAMS AND PERFORMANCE EVALUATION OF SILANE IN CONCRETE BRIDGE DECKS

Major Field: Civil Engineering

Biographical:

Education:

Completed the requirements for the Master of Science in Civil Engineering at Oklahoma State University, Stillwater, Oklahoma in May, 2020.

Completed the requirements for the Bachelor of Science in Civil Engineering at National University of Sciences and Technology, Islamabad, Pakistan in 2016.

Experience:

Graduate Research Assistant, Oklahoma State University, Stillwater, Oklahoma
Aug 2018 – May 2020

Project Engineer, Ali Zaman Private Limited, Lahore, Pakistan.
Dec 2017 – June 2018

Professional Memberships:

American Society of Civil Engineers (ASCE)

American Concrete Institute (ACI)

American Institute of Steel Construction (AISC)